Predicting ion concentration polarization and analyte stacking/focusing at nanofluidic interfaces

Fatima Flores-galicia, Eden Alexander, Antoine Pallandre, Sumita Pennathur, Anne Marie Haghiri-Gosnet

Predicting ion concentration polarization and analyte stacking/focusing at nanofluidic interfaces

Fatima Flores-Galicia[a*], Alexander Eden[b*], Antoine Pallandre[c],

Sumita Pennathur[b] and Anne-Marie Haghiri-Gosnet[a].

[a] Université Paris-Saclay, CNRS, Centre de Nanosciences et Nanotechnologies, UMR9001, 91120 Palaiseau, France
[b] Department of Mechanical Engineering, University of California Santa Barbara, Santa Barbara, CA 93106, USA
[c] Université Paris-Saclay, CNRS, Institut de Chimie Physique, UMR8000, 91405 Orsay, France

[*]**Corresponding authors:**
Ms. Fatima Flores-Galicia, Université Paris-Saclay, CNRS, Centre de Nanosciences et Nanotechnologies, UMR9001, 91120 Palaiseau, France. Email : fatima.flores-galicia@c2n.upsaclay.fr
and
Dr. Alexander Eden, Department of Mechanical Engineering, University of California Santa Barbara, Santa Barbara, CA 93106, USA. Email: a_eden@ucsb.edu

Please insert ORCIDs for the following authors:

Antoine Pallandre: https://orcid.org/0000-0002–7300–7874

Sumita Pennathur: https://orcid.org/0000-0003-2227-4005

Anne-Marie Haghiri-Gosnet: https://orcid.org/0000-0001–7514-244X

Keywords: 2D COMSOL Multiphysics® simulations / Electrokinetic transport / Ion concentration polarization / Nanofluidics

Abbreviations: CF, cathodic focusing; **CS**, cathodic stacking; **EDL,** electrical double layer; **EK**, electrokinetics; **EN**, electroneutrality; **EP**, electrophoretic migration

Abstract: We report on the investigation of electropreconcentration phenomena in micro/nanofluidic devices integrating 100 μm long nanochannels using 2D COMSOL simulations based on the coupled Poisson–Nernst–Planck and Navier–Stokes system of equations. Our numerical model is used to demonstrate the influence of key governing parameters such as electrolyte concentration, surface charge density, and applied axial electric field on ion concentration polarization (ICP) dynamics in our system. Under sufficiently extreme surface-charge-governed transport conditions, ICP propagation is shown to enable various transient and stationary stacking and counter-flow gradient focusing mechanisms of anionic analytes. We resolve these spatiotemporal dynamics of analyte and electrolyte ICP over disparate time and length scales, and confirm previous findings that the greatest enhancement is observed when a system is tuned for analyte focusing at the charge-excluding microchannel-nanochannel electrical double layer (EDL) interface. Moreover, we demonstrate that such tuning can readily be achieved by including additional nanochannels oriented parallel to the electric field between two microchannels, effectively increasing the overall perm-selectivity and leading to enhanced focusing at the EDL interfaces. This approach shows promise in providing added control over the extent of ICP in electrokinetic systems, particularly under circumstances in which relatively weak ICP effects are observed using only a single channel.

Additional supporting information may be found online in the Supporting Information section at the end of the article.

Color online: See article online to view Figs. 1–5 in color.

1 INTRODUCTION

Micro- and nanofluidic devices based on ion concentration polarization (ICP) have been widely developed in recent decades, particularly in the context of protein and DNA separation and detection, analyte preconcentration and the study of enzymatic reaction kinetics [1–4]. In such nanofluidic devices, separation, concentration and detection of analytes can be obtained simultaneously under electric field stimuli using ICP-based focusing techniques. Typically, ICP is induced across nanochannels or membranes that play the role of ion-selective filters between microchannels. In low ionic strength regimes, in which electric double layers (EDLs) are insufficient to fully screen the electric field arising from the interfacial surface charge, co-ionic species are electrostatically excluded to some extent from the nanochannel or membrane. Under the influence of an applied electric field, this charge exclusion and the competition between electroosmotic flow (EOF) and electrophoretic migration (EP) lead to unbalanced ionic transport between anionic and cationic species of a background electrolyte (BGE) solution across the microscale-nanoscale interface. The result is a "polarization" of the concentration distribution, in which BGE ions are depleted on one side of the nanochannel and accumulate at the other [5]. This enrichment-exclusion effect generates zones of ionic solution with high and low conductivity on opposite sides of the channel; these conductivity gradients and the corresponding gradients in the local electromigration velocity of analytes produce counter-flow stacking/focusing phenomena of analytes at or near the enrichment and depletion interfaces.

ICP was first experimentally observed by Pu et al. [6] and later described in detail theoretically by Mani et al. [7] and Zangle et al. [8] in conventional nanofluidic devices that integrate a large horizontal nanochannel between two micro-reservoirs. Based on this general analytical theory [7,8], two key parameters governing the mechanisms for ICP were identified: (1)

the inverse Dukhin number $1/Du$, which describes the ratio of bulk conductivity to surface conductivity, and (2) the dimensionless co-ion mobility v_-^* defined as the electrophoretic velocity of the co-ion (to the wall charge) nondimensionalized by the electroosmotic velocity. Two operating regimes appear at the extrema: (i) for $1/Du \gg 1$ (low surface conductance) and low v_-^* values, ions will weakly accumulate at one micro-nano interface and be depleted at the other in a regime called "CP without propagation," and (ii) for $1/Du \ll 1$ (high surface conductance), significant ion accumulation and depletion "shocks" can form and extend into the reservoirs some distance away from the respective interfaces in a regime called "propagating CP" [8].

To better understand the mechanisms of preconcentration inside micro- and nanofluidic devices, several theoretical studies based on multiphysics finite elements analysis have been undertaken, with most studies implementing the Poisson–Nernst–Planck and Navier–Stokes system of equations to couple transport equations and predict ionic fluxes. In 2008, A. Plecis et al. [9] proposed the first 1D model within a commercial finite element code that evidences the two previously-mentioned operating regimes in the context of analyte preconcentration. They showed that a stable focal frontline can be obtained for a specific range of surface charge and electric field magnitudes between the stacking regime at low surface charge (i.e., with $1/Du \gg 1$) and the propagating regime at high surface charge ($1/Du \ll 1$). This study further highlighted the strong dependence of such processes on the nature of the preconcentrated molecules, with enrichment factors dependent on both the diffusion coefficient and the valence of the analyte. In a separate work, Wang et al. [10] studied ion transport of background electrolytes and analytes in nanochannels upon applying an external hydrodynamic force, and demonstrated that ICP enrichment-exclusion effects can manifest alongside streaming potentials when fluid transport is driven mechanically (rather than electrically) in finite-EDL nanochannels. Numerical simulations

have also been performed in different geometries, including embedded perm-selective membranes [11,12] and novel nanochannel structures [13,14]. Liu et al. [15] investigated the mechanisms of ion transport through micro-nanochannel interfaces for desalination and micromixing, whereas Gong et al. [16] presented numerical simulations of a new microfluidic system based on ICP for purification purposes. Biologically relevant simulations in simple channels were also developed by Dubsky et al. [17] to investigate ICP of DNA molecules as a plug of immobilized anions.

In addition to numerical studies, many microfluidic-based methods have been used for preconcentration of analytes on-chip, such as ion concentration polarization focusing (ICPF) [18–20] and periodic ICP [21]. A common fluidic architecture encountered in ICP-based preconcentration devices is one with a continuous microchannel and orthogonally oriented nanochannels branching away from the microchannel, wherein one applied field drives transport through the microchannel and another induces ICP across the nanochannels to form an extended depletion zone in the continuous microchannel [1,2,4,11,15,16,19,22]. While this architecture is more tunable and can achieve higher ($\sim 10^6 - 10^7$) preconcentration factors than straight channels connecting two reservoirs, its fabrication and operation are more complex, and its somewhat specialized design is less common to non-preconcentration-based nanofluidic applications where ICP still plays a role. The recent work of J. Han's group [22] has called attention to the importance of the role of the concentrated analyte as a charge carrier in the system in such orthogonally-oriented devices with large concentration enhancement factors, and they revealed two distinct operating regimes as a result of their derived scaling laws, simulations, and experiments. In their theoretical and experimental study, Han and coworkers demonstrated that when electrokinetic trapping and the resulting preconcentration are weak, a dilute analyte will remain at such a low concentration relative to the BGE ions that its enhancement does not affect the electrical and

hydrodynamic forces that drive the accumulation; in this electrokinetics (EK) governed regime, the analyte concentration enhancement factor is therefore independent of the initial analyte concentration. If the accumulated analyte concentration starts to approach that of the charge-carrying BGE ions, however, the electrokinetics of the system become disturbed and the accumulating analyte will displace BGE ions of the same charge due to electroneutrality (EN). In this EN-limited regime, the maximum concentration of the analyte is limited by the highest concentration the corresponding counter-charged BGE ion can achieve in the preconcentration zone. We will show that, despite differences in the geometry and nature of the preconcentration in our straight-channel device, similar limiting behavior to that reported in ref. [22] is predicted in our system as an anionic analyte preconcentrates directly at the microchannel-nanochannel enrichment interface.

This paper is organized as follows. In section II, we present the two-dimensional (2D) numerical model along with the boundary conditions and numerical mesh discretization, which is adapted based on the initial BGE concentration. In section III, we first discuss the extent of ICP in confined micro-nano-micro fluidic structures under different conditions, and demonstrate that BGE (namely KCl) concentration, native surface charge density and electric field are predictably among the main pertinent parameters governing ICP-related phenomena. In this section, we also discuss our simulation results in the context of the propagating ICP analysis of Mani et al. [7] and Zangle et al. [8]. We then study electropreconcentration of anionic analytes in this nanofluidic ICP environment; at low BGE ionic strength, simulations of spatiotemporal concentration of an anionic analyte reveal different enhancement mechanisms and locations of the preconcentration front that are dictated by the mobility of the analyte. In agreement with the findings of ref. [22], we show a transition from an EK-governed to an EN-limited regime as the initial analyte concentration is

increased and it starts to become a significant charge carrier when accumulated. Finally, we show that in cases with relatively weaker ICP effects, arraying multiple nanofluidic channels in parallel can enhance the overall charge-selectivity and improve the efficacy of stacking/focusing a given analyte. For example, our results predict a shift in the observed preconcentration mechanism at the nanochannel outlet from stacking to focusing, along with an accompanying 40% increase in the maximum analyte concentration, by simply introducing two additional nanochannels in parallel. Effectively tantamount to increasing the pore density and subsequent micro-to-nanoscale interfacial area in a nanoporous system, this approach provides an additional measure of flexibility in designing and tuning electrokinetic ICP systems, particularly if other conditions (e.g., solution environment, nanochannel depth, electric field limits) are constrained.

2 THEORETICAL AND NUMERICAL FRAMEWORK

2.1 The nanofluidic structure

The geometry of the system used for simulations is presented in Figure 1. It consists of a short nanochannel that connects two microchannels considered as reservoirs. The reservoirs have a length L_r of 300 μm and a width W_r of 5 μm. The 100 μm long nanochannel has a width W_n of 100 nm.

The initial electrolyte concentration $c_{0,BGE}$ and the surface charge density σ_S ranges of the micro/nanochannel are estimated using the theory in ref. [23] for a bare glass surface. This surface chemistry equilibrium model considers the concentration of the electrolyte solution $c_{0,BGE}$, pH, the chemical equilibrium constants, the Stern layer properties. The surface charge density σ_S is a function of the electrolyte solution conditions; therefore, for an initial concentration $c_{0,BGE}$ with given pH, it is possible to estimate the corresponding theoretical surface charge density and zeta

potential. As the pH of the electrolyte solution increases, the surface charge density and the zeta potential of glass, for example, become more negative as a higher number of terminal silanol groups are deprotonated. For the following simulations, the initial concentration $c_{0,BGE}$ is varied between 50 µM and 1mM, whereas the imposed surface charge density values σ_S ranged from -0.1 mC/m^2 and -2.5 mC/m^2, within the ranges of reported surface charge of polydimethylsiloxane (PDMS) [24] and glass [25] and in agreement with theoretical values for pH ≤ 6.5 [23]. The choice of appropriate concentration and surface charge densities is also relevant to the convergence of simulations.

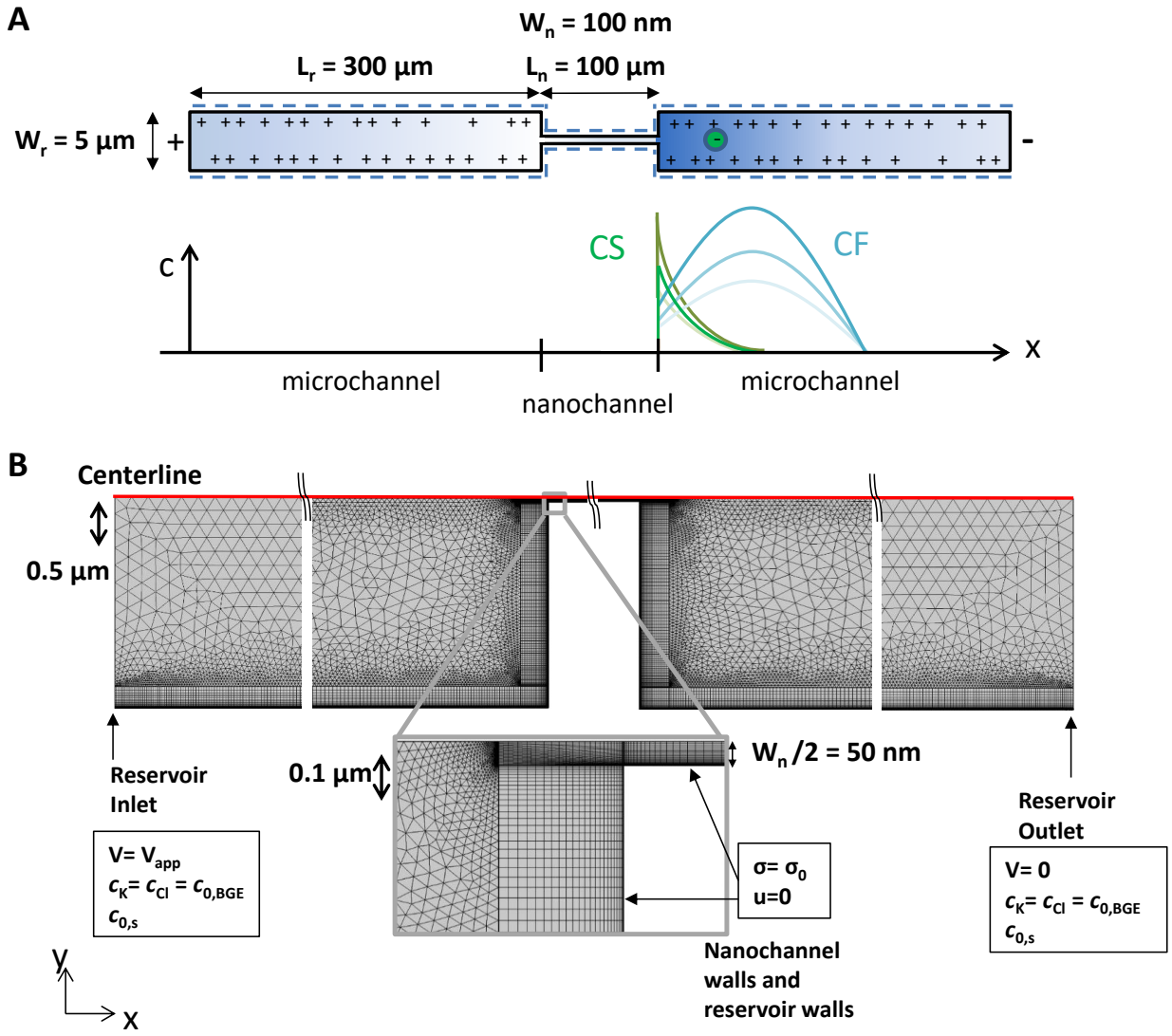

Figure 1. A Schematic side view of the "micro/nano/micro" device with typical dimensions and a schematic variation of anionic analyte concentration profiles evolving via ICP; B Mesh and boundary conditions used for numerical simulations. Dimensions in x are not to scale and represent four segments of the total structure. Because of the axial symmetry of the structure and to render simulations more efficient, a symmetry condition is imposed along the centerline of the channels.

2.2 The 2D numerical model.

The Poisson equation, the Nernst–Planck equation and the Navier–Stokes equation are coupled to study the ion transport within the system under the influence of advection, diffusion, and electromigration.

The Poisson equation (Eq.1) is used to resolve the mean-field electrostatic potential ϕ throughout the electrokinetic system, from which electric field can be obtained using $\mathbf{E} = -\nabla\phi$:

$$-\epsilon_0\epsilon_r\nabla^2\phi = \rho_e. \tag{1}$$

Here, ε_r and ε_0 are the relative permittivity (assumed to be uniform) and the vacuum permittivity, respectively, and ρ_e is the volumetric charge density. For a system with n species in solution, ρ_e is given by:

$$\rho_e = F\sum_{i=1}^{n} z_i\, c_i, \tag{2}$$

where F, z_i, and c_i are, respectively, the Faraday constant, the ion valence and the molar concentration of species i.

The local potential ϕ is set to be equal to an applied potential at left boundary of the inlet reservoir and grounded at right boundary of the outlet reservoir. A common surface charge boundary condition is used at the negatively charged walls of both nanochannel and reservoirs to define the normal displacement field component at the edge of the EDL diffuse layer.

The Nernst–Planck equation (Eq.3) is applied to determine the ion concentration distributions,

$$\frac{\partial c_i}{\partial \mathrm{t}} = -\boldsymbol{\nabla} \cdot [\mathbf{u} c_i - D_i \boldsymbol{\nabla} c_i - \mu_i z_i F c_i \boldsymbol{\nabla} \phi], \tag{3}$$

where μ_i and D_i are the electrophoretic mobility and diffusivity, respectively, of each species, and **u** is the fluid velocity vector. The terms on the right-hand side of Eq. 3 respectively represent the contributions of ion transport due to advection, diffusion and electromigration of ions in the structure. Eq. 3 applies to both background electrolyte and sample species. Here, ion mobilities are obtained from the Nernst–Einstein equation $\mu_i = \frac{D_i}{RT}$ where R is the universal gas constant and T is the solution temperature. We consider a dilute binary BGE solution where c_+ is the cation concentration and c_- is the anion concentration. At the microchannel inlet and outlet boundaries, these concentrations are fixed at the initial concentration of the bulk background electrolyte $c_{0,\mathrm{BGE}}$ ($c_+ = c_\mathrm{K} = c_- = c_\mathrm{Cl} = c_{0,\mathrm{BGE}}$). Similarly, the sample species concentration $c_{0,\mathrm{S}}$ is also specified as equal to the initial sample concentration at the far reservoir boundaries.

The incompressible Navier–Stokes equation with an electrical body force ($-\rho_\mathrm{e}\boldsymbol{\nabla}\phi$), along with the continuity equation, (Eq. 4) are used to solve for the fluid flow,

$$\rho\left(\frac{\partial \mathbf{u}}{\partial t} + \mathbf{u} \cdot \nabla\, \mathbf{u}\right) = \eta \nabla^2 \mathbf{u} - \boldsymbol{\nabla} P - \rho_e \boldsymbol{\nabla}\phi; \quad \nabla \cdot \mathbf{u} = 0, \tag{4}$$

where ρ, t, **u**, P and η are the fluid density, time, fluid velocity vector, the pressure within the fluid and the dynamic viscosity of the fluid, respectively. A no slip condition **u** = 0 is imposed at the nanochannel and reservoir walls.

Numerical simulations were performed using COMSOL© v5.6. In this paper, potassium chloride (KCl) is chosen as a representative BGE and the electrophoretic mobility of the anionic

analyte is varied by changing the diffusion coefficient within the range 0.1×10^{-9} m^2/s – 2×10^{-9} m^2/s (with D= 0.42×10^{-9} m^2/s [26-27] representing Fluorescein, for example).

The mesh was constructed such that control domains are employed near the charged walls to resolve the electrical double layers [28]; the size of these control domains changes depending on the initial concentration of the background electrolyte, ensuring that regions near the walls and in the nanochannel have a sufficiently fine mesh compared with the elements in the rest of the reservoir domains. To render simulations more efficient, we exploited the inherent centerline symmetry of the geometry and only modeled half of the structure.

3 Results and discussion

3.1 Studying ICP effects of the BGE as function of initial concentration, electric field and surface charge density

Mani et al. [7] and Zangle et al. [8] were the first to propose a general analytical theory describing ICP mechanisms. They found that ICP of the BGE is mainly governed by two key parameters: an inverse Dukhin number $1/Du$, which describes the ratio of bulk conductivity to surface conductivity and is defined as $\frac{1}{Du} = \frac{G_{bulk}}{G_\sigma}$, and a dimensionless mobility ν_-^*, defined as the ratio of the electrophoretic velocity of the co-ion (e.g., Cl^- for a BGE of KCl and negatively charged walls) to the electroosmotic velocity. They also noted that ICP depends primarily on the inverse Dukhin number and not necessarily on the ratio of channel size to Debye length, despite the frequent invoking of this quantity as a key governing parameter in the literature; that is, it is not necessary to have "overlapped EDLs" corresponding to a channel size to Debye length ratio of order unity for ICP effects to be present, but rather ICP can be observed for systems with such ratios exceeding 10 [8].

To predict and analyze ICP effects, we first estimate the ratio of bulk conductivity to surface conductivity $1/Du$ and the normalized velocity of co-ion Cl^- v_-^* as a function of both BGE concentration $c_{0,BGE}$ and the surface charge density, as detailed in supplementary information SI.1. The KCl BGE concentration $c_{0,BGE}$ was varied in the range 50 μM – 1 mM; for example, for W_n = 100 nm and σ_S = –2.5 mC/m^2, $1/Du$ varies from 0.195 at $c_{0,BGE}$ = 50 μM to 3.912 at $c_{0,BGE}$ = 1 mM.

One simple way to study how ICP effects vary as a function of $1/Du$ is to compare the Cl^- co-ion concentration profiles in the structure and monitor the manifestation and evolution of depletion and the enrichment zones in each reservoir. Let us, therefore, begin by examining the drift-diffusion of BGE chloride ions inside a 100-nm-wide nanochannel. Figures 2A and 2B respectively show a characteristic 2D depth-averaged view of the co-ion concentration and the steady state normalized concentration profiles for a surface charge density σ_S = –1 mC/m^2, portraying the characteristic ICP depletion and enrichment at the entrance and exit of the nanochannel. When ICP effects are relatively weaker (e.g., at higher electrolyte concentrations and/or lower surface charge densities in the "non-propagating ICP regime" [7]), these enrichment and depletion zones are largely confined to the microchannel-nanochannel interfaces, with diffusion fluxes from the far boundaries capable of balancing the limited enrichment/exclusion effects [7]. As these surface-charge-governed transport effects become more prominent, however, the depletion zone can propagate outward towards the microchannel reservoir boundary. These propagating depletion interfaces (also referred to as shocks) can ultimately travel a distance of up to several hundred of microns from the nanochannel in our modeled system, depending on the bulk BGE concentration $c_{0,BGE}$.

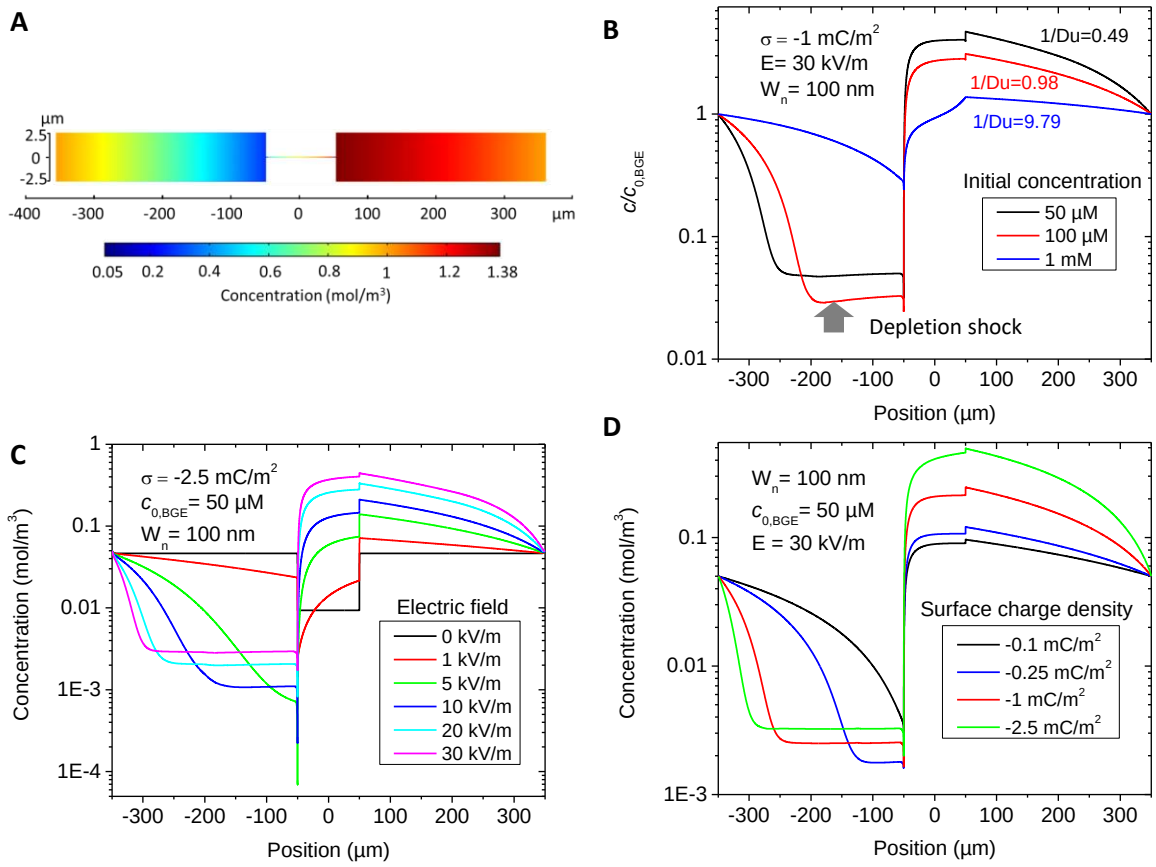

Figure 2. Ion concentration polarization (ICP) effects in KCl solution at the steady state: (A) a typical 2D depth-averaged concentration profile for chloride ions at $c_{0,BGE}$ = 1 mM, and (B) Cl^- concentration profiles obtained along the centerline of the micro/nanochannel structure as function of $c_{0,BGE}$ (50 μM, 100 μM and 1mM) with the electric field fixed at 30 kV/m. The surface charge density σ_S and the nanochannel width W_n are respectively fixed at –1 mC/m² and 100 nm. (C) Visualization of the transition from non-propagating to propagating ICP as the applied electric field is increased (with σ_S = –2.5 mC/m²) and (D) as the surface charge density is varied from –0.1 mC/m² to –2.5 mC/m² (with $c_{0,BGE}$ = 50μM and E=30 kV/m).

At low $c_{0,BGE}$, and thus low $1/Du$ ($1/Du = 0.49$ for $c_{0,BGE}$ = 50 μM and σ_S = –1 mC/m² – black curve in Fig. 2B), a large propagating depletion region can be observed in the anodic reservoir, with an interface located at around 200 μm from the nanochannel entrance. For a concentration $c_{0,BGE}$ = 100 μM (corresponding to moderate $1/Du = 0.98$ – red profile in Fig. 2B),

the depletion zone doesn't propagate as far, instead reaching a distance of 150 μm from the nanochannel entrance, but the zone can be depleted to a greater extent than for $c_{0,BGE}$ = 50 μM because the smaller concentration gradient between this location and the fixed-concentration boundary limits diffusion into the ion-depleted zone. Finally, at higher $c_{0,BGE}$ and thus higher $1/Du$ ($c_{0,BGE}$ = 1 mM and $1/Du = 9.79$ – blue profile in Fig. 2B – non-propagating ICP [7] and EK regime [22]), the depletion is limited and confined to the channel junction, even at a high electric field strength of 30 kV/m. On the cathode side of the nanochannel, enrichment occurs to some extent for all initial concentrations. These simulations confirm that lower $1/Du$ values yield stronger ICP depletion/enrichment effects, in agreement with the theoretical model proposed by Mani et al. [7] and Zangle et al. [8].

Figure 2C evidences the role of the electric field on ICP effects for a typical case (W_n = 100 nm) at low $c_{0,BGE}$ = 50μM and surface charge density σ_S = –2.5 mC/m^2, roughly corresponding to a glass surface and a solution pH of 6.5. At relatively low electric fields (< 5 kV/m) accumulation and depletion zones appear at the ends of the nanochannel, and at around 5 kV/m the depletion zone begins to propagate from the channel junction. Increasing the applied field to 10 kV/m produces propagating ICP with an interface located approximately 125 μm from the nanochannel entrance. Further increasing the field to 30 kV/m leads to an extended depletion zone and higher accumulation at the opposite interface. Even at a fixed $1/Du$ value, the applied electric field has a similarly large impact on ICP as BGE concentration, and only causes propagation when high enough. Figure 2D exhibits the influence of the surface charge density σ_S on co-ionic charge exclusion and the resulting ICP for $c_{0,BGE}$ = 50 μM and an electric field of E= 30 kV/m. Increasing the surface charge density magnitude from –0.1 mC/m^2 to –2.5 mC/m^2 (i.e., going from $1/Du$ = 4.891 to $1/Du$ = 0.195) enhances the enrichment in the cathodic reservoir by five-fold, while the

onset of propagating ICP occurs between –0.1 mC/m^2 and –0.25 mC/m^2 under these conditions. Clearly, both a sufficiently high electric field and low $1/Du$ are necessary to generate strong propagating ICP effects in this single-channel configuration.

3.2 Localization of the preconcentration frontline: role of analyte mobility

At high $1/Du$ values and low ν_-^* values, ICP effects will not propagate and the analyte species cannot enter the channel because electrophoretic migration is insufficient to overcome EOF; the analyte will thus weakly accumulate at the entrance of the nanochannel [7]. Such interfacial accumulation is difficult to utilize in practical preconcentration applications since the concentrated analyte is confined at the nanochannel entrance and will dissipate upon removal of the applied field. On the opposite end of the spectrum, at high Dukhin numbers, the analyte will concentrate at varying locations within the accumulation zone (cathodic reservoir) or stack/focus at the interface of the propagating depletion shock (anodic reservoir) [8, 29]. We have previously shown based on 1D computations in large horizontal nanochannels [9] that an anionic analyte, such as fluorescein (D = 0.42x10^{-9} m^2/s), in a very dilute BGE concentration $c_{0,\mathrm{BGE}}$ = 10 µM ($1/Du = 0.098$), will concentrate in the cathodic reservoir in an electrophoretically-dominated regime. Such low ionic strengths gave rise to cathodic concentration profiles that were unstable over time, however, owing to the propagating ICP dynamics of the BGE [8]. In this context, studying the BGE propagation and subsequent analyte preconcentration regimes and mechanisms in our micro/nano/micro structure is of great interest.

In this section we investigate how diluted dianionic analytes (valence z = –2 and $c_{0,\mathrm{S}}$ = 10^{-9} M) with different mobilities $\mu_i = \frac{D_i}{RT}$ concentrate under the conditions studied in the previous section ($c_{0,\mathrm{BGE}}$ = 50 µM, W_n = 100 nm and E = 30 kV/m – green curve in Figure 2D). Figure 3 presents the evolution of normalized concentration profiles of a dilute analyte being transported

through a 100 nm wide nanochannel with two different surface charge densities (-1 mC/m^2 and -2.5 mC/m^2) for a range of sample mobilities.

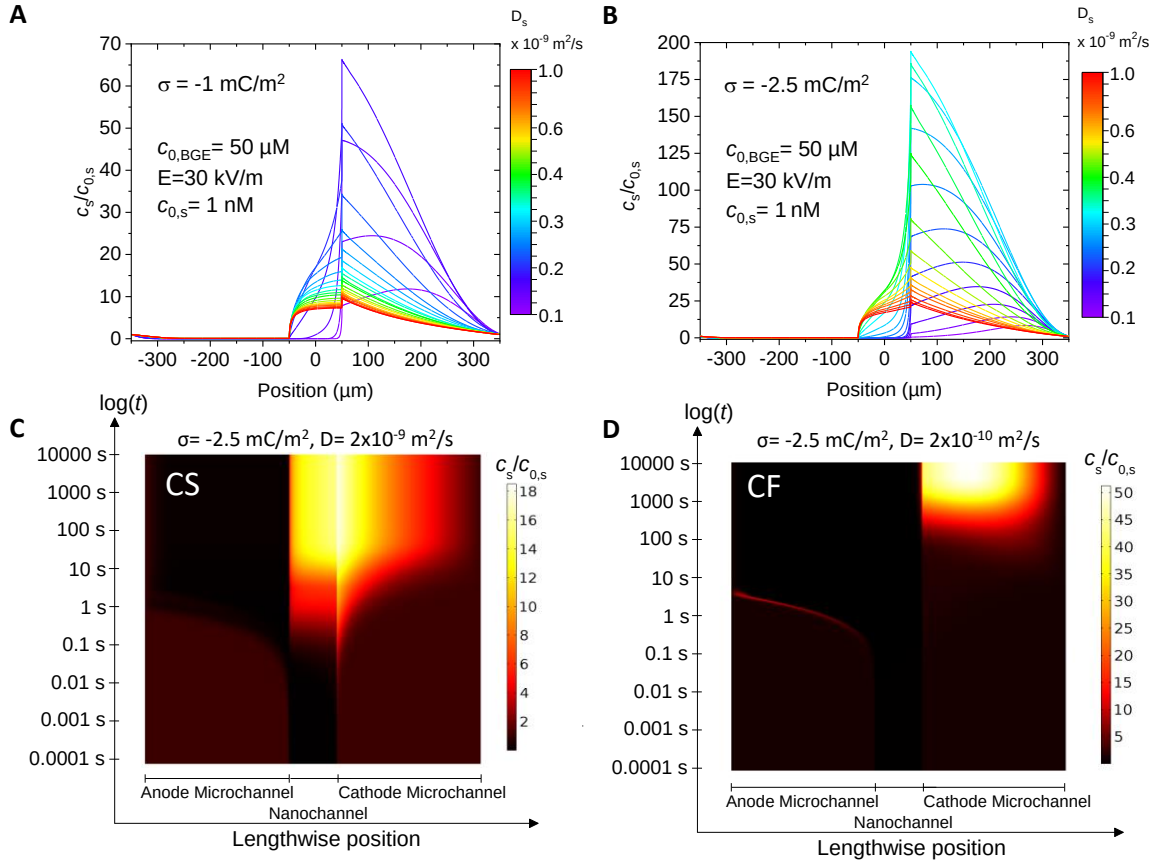

Figure 3. Evolution of the normalized concentration profiles with analytes of different diffusivity for two surface charge densities, (A) -1 mC/m^2 and (B) -2.5 mC/m^2. For both figures, the initial bulk BGE concentration is 50 µM, the initial bulk concentration of the analyte is 1x10^{-9}M and the applied electric field is 30 kV/m. The spatiotemporal evolution of the normalized centerline concentration profiles is shown via time-extrusion plots for two analytes with diffusion coefficients of (C) 2x10^{-9}m^2/s and (D) 2x10^{-10} m^2/s and a surface charge density of -2.5 mC/m^2. The vertical axis for the time-extrusion plots is logarithmic in time, revealing dynamics of BGE ICP propagation as well as various stacking and focusing analyte enhancement mechanisms occurring over many temporal orders of magnitude.

In Figure 3A, corresponding to a surface charge density of -1 mC/m^2, most of the analytes with mobilities in the depicted range experience accumulation at the nanochannel outlet in a process previously termed cathodic stacking (CS) [9]. Here, any anionic analyte ions that are able to bypass the electrokinetic exclusion/trapping at the transitioning EDL interface (e.g., via diffusion) are still able to travel through the channel towards the anodic reservoir. Thus, a meaningful concentration of sample ions is still visible in the nanochannel. As the diffusion coefficient of the analyte decreases, the concentration enhancement at the entrance of the nanochannel increases as the sample finds it more difficult to enter and ultimately be transported through the channel. Beyond a critical mobility value (specific to the conditions and extent of ICP observed), the sample is no longer able to migrate through the channel and will instead be driven to a common point of zero net velocity from both sides of the interface. This cathodic focusing (CF) phenomenon provides the highest rate of analyte enrichment when the focusing location coincides with the microchannel-nanochannel interface; however, for lower mobility samples, the electric field gradient associated with the accumulation-depletion zones causes this counter-flow gradient focusing location to shift away from the charge-selective interface into the microchannel, leading to a weaker enhancement effect. For a surface charge density of -2.5 mC/m^2, Figure 3B predicts maximum interfacial CF for dianionic analytes with a diffusivity around 0.35×10^{-9} m^2/s.

To further investigate the CS and CF mechanisms, we resolve the spatiotemporal propagating ICP dynamics of the BGE and analyte over many temporal orders of magnitude by implementing a logarithmic time discretization. This enables us to start from a condition with equilibrium EDLs and concentration distributions before very rapidly introducing an applied field and observing the evolution of the electrokinetic transport dynamics over an extended period until a steady state is reached.

Figures 3C and 3D depict a logarithmic time-extrusion of the centerline sample concentration for analytes with diffusivities of 0.2×10^{-9} m^2/s and 2×10^{-9} m^2/s; that is, the profiles are colorized and stacked vertically to create a horizontal position axis and a vertical log(time) axis. As the 2×10^{-9} m^2/s sample essentially has the same diffusivity as the KCl BGE ions [28], the ICP dynamics of these sample ions mirror those of the evolving BGE ion distributions that govern the fluid flow and electric fields. The depletion region is observed to grow linearly in time, in agreement with experimental findings [8] (note again that the plotted time axis is logarithmic), as the depletion front propagates from the channel interface to its ultimate steady state position approximately 250 μm from the nanochannel entrance. The accumulation region also grows linearly in time, though at a slower rate than the fast-moving depletion zone, which generates a large local electric field and subsequently experiences a higher front propagation velocity. The visible charge exclusion of the analyte from the nanochannel at very early times quickly gives way to an increase in concentration as a CS profile develops at the nanochannel outlet and diffusion allows these more mobile ions to overcome the charge exclusion effects to enter and then migrate through the channel.

For a less mobile sample with a diffusivity of 0.2×10^{-9} m^2/s, Figure 3D predicts that preconcentration will manifest in both microchannels, though at different time scales. As the BGE concentration distribution evolves due to ICP, the transport of the sample ions will be significantly influenced by the propagating depletion front. Specifically, the large electric field in the ion-depleted zone causes sample ions at the leading edge of the front to migrate at a high electrophoretic velocity. Just ahead of the front (i.e., farther away from the nanochannel), the electric field and subsequent local transport of ions is reduced, causing the faster moving ions behind to stack and increase the local concentration as the depletion zone spatiotemporally

propagates. This anodic stacking effect is short-lived, however, and dissipates within 10 seconds as the depletion interface reaches its steady state location close to the microchannel boundary. In contrast to Figure 3C, this lower mobility anionic sample cannot enter the channel on the cathodic side due to the competition between EOF and weaker EP, thus the entire nanochannel remains depleted of sample ions. The focusing interface and subsequent location of maximum concentration for this sample is shifted slightly away from the cathodic microchannel/nanochannel interface, such that the enhancement is purely that of a more conventional focusing phenomenon rather than also being influenced by the electric field associated with the charge-selective transitioning EDL interface.

By analyzing the spatiotemporal dynamics for samples of varying mobility, one can identify useful regimes for preconcentration and tune the design and/or operating conditions of a given system to maximize the enhancement of a given analyte. Figure 3 demonstrates that, if a static preconcentration front is desired (e.g., for detection purposes), the greatest level of enrichment will occur when the system is tuned for CF at the microchannel-nanochannel interface.

3.3 Role of the initial analyte concentration on maximum achievable preconcentration

Following the analysis of Ouyang et al. [22], we investigate the influence of the sample analyte concentration on the maximum achievable preconcentration in our straight-channel system. In ref. [22], the authors identified two distinct regimes of preconcentration in their straight microchannel/orthogonal nanochannel device, with behavior dependent on the maximum accumulated analyte concentration relative to the BGE ions; they identified what they termed an "electrokinetics" (EK) governed regime and an "electroneutrality" (EN) limited regime. In the EK

regime, the dilute analyte is at such a low concentration relative to the BGE ions everywhere that its contribution to the overall charge transport is negligible, and thus the resulting electric field and flow distributions which determine the balance of forces on the analyte are unaffected as it accumulates; the background flow and electric field can be thought of as "static" and the corresponding flux balance determines the extent of preconcentration. When the analyte is preconcentrated to levels where it approaches the BGE ion concentrations, however, it can become a significant charge carrier and affect the system electrokinetics as it accumulates. Indeed, as an anionic analyte concentrates, for example, it must displace other anions in the preconcentration zone in order for overall electroneutrality to be maintained. Therefore, in this EN-limited regime, the analyte will be unable to accumulate to higher concentrations than that dictated by the maximum BGE cation concentration achieved in the enrichment zone. Despite the fact that the preconcentration in Ouyang et al. occurs on the anodic side of the nanochannel at the edge of the depletion zone – as opposed to the stacking/focusing directly at the cathodic microchannel-nanochannel interface shown in this work – similar limiting behavior governs our straight-channel system.

In Figure 4A and 4B below, we depict the steady state BGE and analyte ion concentration distributions along the system centerline for the cases of (A) a near-insignificant initial analyte concentration of 1 nM (relative to a 50 μM nominal KCl concentration; note that the initial Cl^- concentration is reduced by 2x the initial dianionic sample concentration in order to satisfy bulk electroneutrality) and (B) a non-negligible initial concentration of 2 μM. With a very dilute initial concentration of 1 nM, the sample analyte concentration in the enrichment zone remains sufficiently small to have minimal influence on the BGE electrokinetics and overall charge transport (EK regime). When the initial concentration is increased to 2 μM, the accumulated

dianionic analyte ions at the cathodic microchannel-nanochannel interface displace anions and begin to influence the electric field distribution and ICP dynamics, limiting the maximum achievable concentration as the EN limit is approached in our system. Figure 3C shows that the 1 nM condition remains in the EK regime, as evidenced by the exponential increase in preconcentration factor with increasing applied voltage, while the preconcentration for a 15 µM analyte begins to plateau as the EN limit is approached. Figure 4D clearly demonstrates this transition, with concentration-independent preconcentration in the EK regime below approximately 1 nM, and a rapidly decreasing maximum concentration ratio as the analyte approaches the concentration limited by EN (specifically, the stacked BGE cation concentration at the cathodic enrichment interface).

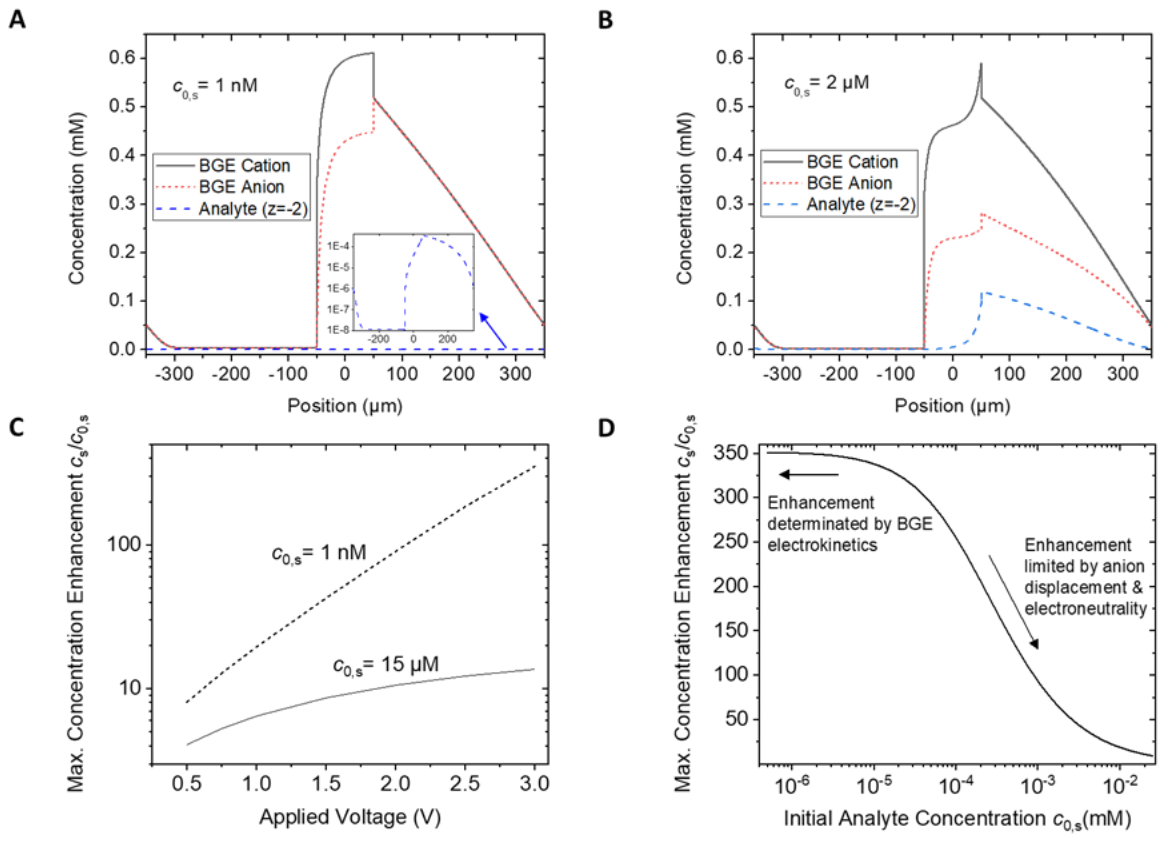

Figure 4. Role of the initial sample analyte concentration on the background electrolyte ions and achievable preconcentration for 50 μM KCl, $\sigma_S = -2.5$ mC/m^2, E = 30 kV/m (for A, B, D), W_n = 80 nm, and a sample with a diffusivity of 3.25x10^{-10} m^2/s. (A) Ion distributions with a very dilute initial sample concentration of 1 nM show conventional ICP behavior in the EK regime, with the BGE ion concentrations indifferent to the accumulating analyte. (B) Ion distributions for a higher initial sample concentration of 2 μM demonstrate how accumulating dianionic analyte ions at the nanochannel interface displace BGE anions as the electroneutrality-limited regime is approached. (C) Concentration enhancement for a 1 nM analyte shows an exponential increase with preconcentration at higher applied voltages, while the enhancement of a 15 μM analyte starts to saturate as the EN limit is approached. (D) The transition from EK to EN regimes is apparent from the decrease in preconcentration as the initial analyte concentration is increased to 25 μM, where it fully displaces all BGE anions in solution.

3.4 Role of the number of nanochannels involved in preconcentration

In an effort to bridge the insight gap between the conventional single nanochannel systems previously studied [7–9,13] and those employing nanoporous membranes or frits [11,12], we investigate the effect of including additional nanochannels between the two microchannels. This effectively amounts to increasing the pore density in a nanoporous material, such that the overall perm-selectivity is enhanced by increasing the interfacial area that promotes charge exclusion and surface-charge-governed transport; this approach can be particularly useful for situations in which the device or operating conditions are constrained such that large Dukhin numbers cannot be readily achieved (e.g., if fabrication capabilities limit the minimum attainable nanochannel size,

or if a higher concentration buffer is needed due to a salt-requiring bioanalyte), and provides added design flexibility in the form of the geometric architecture.

As BGE ion depletion zones form and propagate, they naturally have a substantial impact on the potential distribution and local electric fields throughout the system. The large potential drop associated with an extended depletion region in one of the microchannels attenuates the average electric field within the nanofluidic channel, while the local field distribution is also influenced by the concentration gradient between the enriched and depleted reservoirs; the resulting conductivity gradient generates a nonuniform electric field along the channel that dictates the competition between EOF and electrophoretic migration of analyte ions trying to enter the channel from the enriched cathodic reservoir. By adding additional nanochannels in parallel between the microchannels, this competition can be tuned without changing any other parameters.

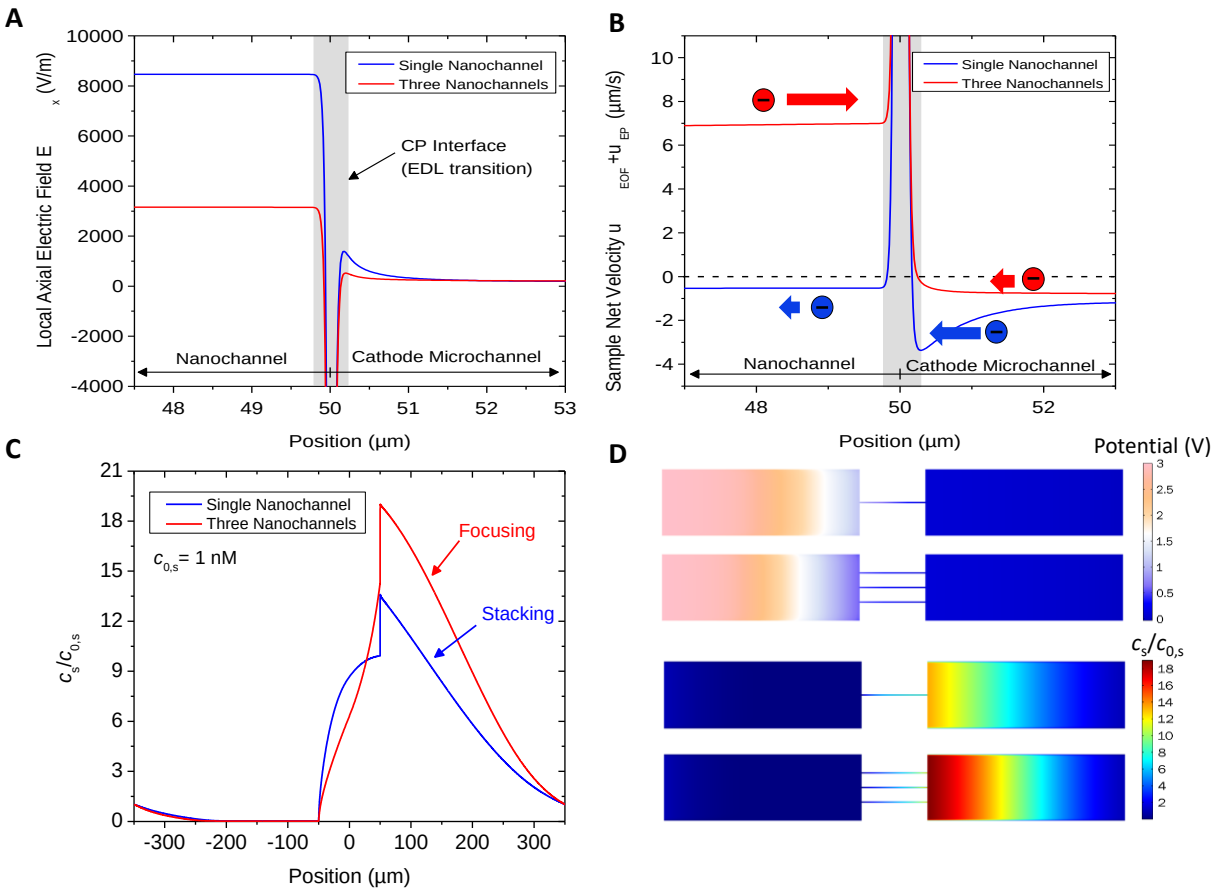

Figure 5. ICP for a single nanochannel versus three parallel nanochannels for 50 μM KCl, $\sigma_S = -0.5$ mC/m^2, E = 30 kV/m, W_n = 100 nm, and a sample with a diffusivity of 1.33x10^{-10} m^2/s. (A) Local electric field and (B) corresponding sample net transport velocity (EOF + EP) near the nanochannel/cathodic microchannel interface for a single nanochannel (blue) and three parallel nanochannels (red). (C) Normalized concentration profiles show a transition from a stacking profile with one nanochannel to a focusing profile with three nanochannels due to the change in electric field and ion transport velocity depicted in B. (D) 2D depth-averaged concentration and electric potential distributions for one and three nanochannel configurations demonstrate stronger ICP effects and subsequent preconcentration arising from the addition of multiple parallel channels.

Figure 5A shows the local axial electric field distribution near the nanochannel/cathodic microchannel interface, at which BGE ions accumulate and reduce the local field strength. Results

are shown for 50 μM KCl, σ_S = –0.5 mC/m^2, E = 30 kV/m, and W_n = 100 nm (corresponding to $1/Du = 0.98$). Within approximately 250 nm on either side of the nanochannel outlet, the EDL transitions from an overlapped EDL inside the channel to a near-electroneutral solution region in the cathodic microchannel, forming an electrostatic exclusion zone due to the transitioning EDL potential and its associated field. When a single nanochannel is replaced with three parallel channels, the enhanced overall charge-selectivity of the system and subsequent ICP effects lead to a further reduction in the field near the outlet. For a dianionic sample with a diffusivity of 1.33x10^{-10} m^2/s, the single nanochannel case yields a local field acceptably high for sample ions to enter the nanochannel, and stacking across the ICP interface is observed due to the relatively low (but still negative) ion transport velocity in the channel. With three parallel nanochannels, however, the field is reduced sufficiently to prevent these ions from entering any of the nanochannels via migration, and they are instead driven from both sides to the ICP focusing interface at the channel outlets. This transition from interfacial stacking to focusing yields a 40% increase in the preconcentration ratio $c_S/c_{0,S}$ under these conditions, as shown in Figure 5C. Figure 5D shows a 2D depth-averaged distribution of the electric potential throughout the system, along with the sample ion concentration, for the cases of both single and three parallel channels. The potential distributions reflect the extended depletion zone and the additional accumulation-depletion induced by increasing the number of parallel channels, both of which serve to reduce the electric field near the nanochannel outlets and prevent the sample from entering the three nanochannels.

In addition to more conventional approaches for tuning ICP, the introduction of additional nanochannels in parallel can add greater design flexibility, provide improved cathodic preconcentration for a given set of conditions, and even potentially enable focusing for moderate Dukhin number conditions and analyte dimensionless mobility values nominally above unity.

4 Concluding remarks

Using a 2D COMSOL Multiphysics® numerical model with a parameterized mesh discretization adapted for varying background electrolyte concentrations, we investigated the role of important governing parameters including the BGE concentration, the electric field, the wall surface charge density and the analyte mobility on the ICP dynamics and corresponding preconcentration mechanisms in a microchannel-nanochannel-microchannel system. We first demonstrated the onset and extent of propagating ICP in dilute solution conditions, confirming that both a sufficiently large electric field and a high Dukhin number are necessary conditions in a conventional single-channel configuration for concentration polarization effects to appreciably propagate outwards from the microchannel-nanochannel interfaces [7]. In such cases, a tunable, extended depletion region coupled with a concentration gradient across the nanochannel lead to an attenuated, nonuniform electric field distribution that can be leveraged for stationary analyte preconcentration – either at the charge-selective interface, or at a mobility-dependent counter-flow gradient focusing location.

We illustrated the spatiotemporal evolution of propagating ICP dynamics over disparate time and length scales using a logarithmic time discretization spanning eight temporal orders of magnitude. Our results showed a linear growth in the accumulation and depletion zones over time, in agreement with previous experimental findings [8], and indicate that both transient and stationary stacking and focusing profiles are achievable for anionic analytes of varying mobility, as predicted by 1D simulations [9]. As expected, lower sample mobilities shifted the cathodic preconcentration location away from the nanochannel as the enhancement mechanism transitions from CS to CF at the interface and then weaker CF in the microchannel; the highest preconcentration factor can be observed for CF at the nanochannel EDL interface. We show that

electrokinetics-governed and electroneutrality-limited preconcentration regimes previously evidenced in straight microchannel/orthogonal nanochannel devices [22] also manifest and dictate limiting behavior in our straight-channel system as the analyte concentration increases from a negligible level to one at which it becomes a non-negligible charge carrier capable of appreciably displacing BGE ions.

Finally, we investigated the effect of increasing the interfacial area of the charge-selective microchannel-nanochannel EDL interface by arraying three nanochannels in parallel. We found that this enhances the overall perm-selectivity of the structure, strengthening ICP effects and improving resulting preconcentration capabilities in certain cases; this is analogous to increasing the pore density in a nanoporous membrane, for example. By changing from a single-channel structure to a three-channel configuration, the electric field in the channel became increasingly nonuniform and further attenuated due to extended depletion zone propagation and more strongly polarized accumulation/depletion profiles. This allows for increased control over the competition between EOF and electrophoretic migration as anionic samples try to enter the nanochannels, and enables the transition from a CS preconcentration mechanism to the more effective CF scheme that allows for higher enrichment factors. Such a multi-channel approach provides added flexibility in the design of ICP systems, particularly in situations where the nanochannel size and/or electrolyte concentration have practical limitations which set a minimum achievable inverse Dukhin number and/or analyte mobility. Additional characterization simulations and future experiments with multiple-nanochannel devices will be performed to confirm and expand the efficacy of this versatile approach for tuning and enhancing ICP-based preconcentration.

All authors would like to thank ANR for the financial support (NANOCODE project ANR-18-CE09-0042-01).

The authors have declared no conflict of interest.

Data availability statement

The data that support the findings of this study are available from the corresponding author upon reasonable request.

5 References

[1] Wang, C., Wang, Y., Zhou, Y., Wu, Z.Q., Xia, X.H., Anal. Bioanal. Chem. 2019, 411, 4007–4016.

[2] Choi, J., Baek, S., Kim, H.C., Chae, J.H., Koh, Y., Seo, S.W., Lee, H., Kim, S.J., BioChip J. 2020, 14, 100–109.

[3] Yamamoto, K., Ota, N., Tanaka, Y., Anal. Chem. 2021, 93, 332–349.

[4] Kim, S.J., Song, Y.A., Han, J., Chem Soc Rev. 2010, 39, 912–922.

[5] Schoch, R.B., Han, J., Renaud, P., Rev. Modern Phys. 2008, 80, 839–883.

[6] Pu, Q., Yun, J., Temkin, H.,. Liu, S., Nano Lett 2004, 4, 1099–1103.

[7] Mani, A., Zangle, T. A., Santiago, J. G., Langmuir 2009, 25, 3898.

[8] Zangle, T. A., Mani, A., Santiago, J. G., Chem. Soc. Rev. 2010, 39, 1014–1035.

[9] Plecis, A., Nanteuil, C., Haghiri-Gosnet, A.M., Chen, Y., Anal. Chem. 2008, 80, 9542–9550.

[10] Wang, Y., Pant, K., Chen, Z., Wang, G., Diffey, W.F., Ashley, P., Sundaram, S., Microfluid Nanofluid 2009, 7, 683–696.

[11] Li, Z., Liu, W., Gong, L., Zhu, Y., Gu, Y., Han, J., Int. J. Appl. Mech. 2017, 09, 1750107.

[12] Gholinejad, M., Moghadam, A. J., Shaegh, S.A.M., Miri, A.K., Phys. Fluids 2020, 32, 072012.

[13] Han, W., Chen, X., Appl. Nanosci. 2020, 10, 95–105.

[14] Han, W., Chen, X., J Braz. Soc. Mech. Sci. Eng. 2020, 42, 49.

[15] Liu, W., Zhou, Y., Shi, P., Appl. Nanosci. 2020, 10, 751–766.
[16] Gong, L., Lia, Z., Han, J., Sep. Purif. Technol. 2019, 217, 174–182.
[17] Dubsky, P., Das, S., Van den Berg, A., Eijkel, J. C. T., μTAS 2011, 212–214.
[18] Papadimitriou, V. A., Segerink, L. I., Eijkel, J. C. T., Lab Chip 2019, 19, 3238–3248.
[19] Berzina, B., Anand, R. K., Anal. Chim. Acta 2020, 1128, 149e173.
[20] Papadimitriou, V. A., Segerink, L. I., Eijkel, J. C. T., Anal. Chem. 2020, 92, 4866–4874.
[21] Park, S., Buhnik-Rosenblau, K., Abu-Rjal, R., Kashib, Y., Yossifon, G., Nanoscale 2020, 12, 23586.
[22] Ouyang, W., Ye, X., Li, Z., Han, J., Nanoscale 2018, 10, 15187.
[23] Behrens, S. H., Grier, D. G., J. Chem. Phys. 2001, 115, 6716.
[24] Almutairi, Z., Rena, C. L., Simonc, L., Colloids Surf. 2012, 415, 406–412.
[25] Martins, D. C., Chu, V. J., Conde, P., Biomicrofluidics 2013, 7, 034111.
[26] Casalini, T., Salvalaglio, M., Perale, G., Masi, M., Cavallotti, C., J Phys Chem B 2011, 115, 12896–12904.
[27] Milanova, D., Chambers, R.D., Bahga, S.S., Santiago, J.G., Electrophoresis 2011, 32, 3286–3294.
[28] Eden, A., McCallum, C., Storey, B. D., Pennathur, S., Meinhart C. D., Phys. Rev. Fluids 2017, 2, 124203
[29] Ngom, S.M., Flores-Galicia, F., Delapierre, F.D., Pallandre, A., Gamby, J., Le Potier, I., Haghiri-Gosnet, A.M., Electrophoresis 2020, 41,1617–1626.